Chaotic and regular dynamics of a morphing shell with a vanishing-stiffness mode

Sergio Chibbaro[1], Walid Hamouche[1], Corrado Maurini[1], Stefano Vidoli[2], and Angela Vincenti[1]

[1] *Sorbonne Université, CNRS, UMR 7190, Institut Jean Le Rond d'Alembert, F-75005 Paris, France and*
[2] *Dipartimento di Ingegneria Strutturale e Geotecnica, Sapienza Università di Roma, Italy*

Thin elastic shells are almost inextensible but easy to bend. In the presence of prestresses, geometric frustrations can produce complex elastic energetic landscapes, which have been tailored for the design of morphing structures with multiple stable equilibria or neutrally stable manifolds. We show that the co-existence of stiff and floppy modes leads to unexploited dynamical features. We build a neutrally stable cylindrical shell that under dynamical excitation alternates a chaotic behaviour with a surprisingly regular regimes with a continuous precession of the curvature axis at a constant speed. We explain the experimental findings with a minimal model, showing how the intriguing dynamics is due to the subtle coupling between the prestress, geometrical nonlinearity, material anisotropy and inertial effects. Our results shed a new light on morphing structures dynamics and can be exploited in engineering applications such as energy harvesting.

INTRODUCTION

Slender elastic structures can experience reversible, controllable large shape-changes. The design of *morphing structures*, *i.e.* structures capable to adapt their shape to different functions, have received a large interest in the last two decades, based on the observation of natural phenomena [13, 14] or aiming at production of technological devices [6, 20]. Nowadays a rich gallery of shapeable multistable objects is available, spanning from origami [31] to large scale deployable structures [1].

Because of the interplay between elasticity and geometry, prestressed elastic shells provide a fascinating playground for morphing structure design [27, 28]. Their shape can be controlled by prescribing through active materials or plastic prestress the target metric or curvature. They can exhibit multiple stable equilibrium configurations and a complex nonlinear behavior, which can be controlled by plastic deformation [26], growth [8, 16, 24], thermal effects [5] or other multiphysical couplings [18, 22]. Yet, only few works have investigated their nonlinear dynamic behavior [4, 15]. Bistable structures have interesting applications for the design of energy harvesters in realistic vibration environments, due to their ability to possible self-synchronisations over a broad frequency range [19, 29]. It is has been shown experimentally that when the energy barrier between the energy wells is low, the potential gain for power harvesting ranges between 400% and 600% with respect to standard linear oscillators [12].

In this Letter, we show how the presence of soft bending modes in almost inextensible shells leads to peculiar dynamical properties. We consider thin multistable shells that are obtained by applying a large isotropic plastic curvature to an initially flat disk [17]. Their equilibrium shape is almost cylindrical, and because of the thinness, the shell is almost inextensible. This kind of structures have interesting properties for shape-control [18] and fluid-structure [11] applications. Here, we demonstrate that the interplay of the pre-stress, geometrical nonlinearities, small material anisotropies and inertial effects results into a complex dynamics alternating chaotic and regular responses. In the regular regime, the shell converts a translational excitation in a continuous precession mode characterized by a constant-speed rotation of the curvature axis, see the video in the Supplemental Material [2]. We develop a minimal two-degree-of-freedom model relating the presence of the soft precession mode to geometrical nonlinearities and the prestress, and its

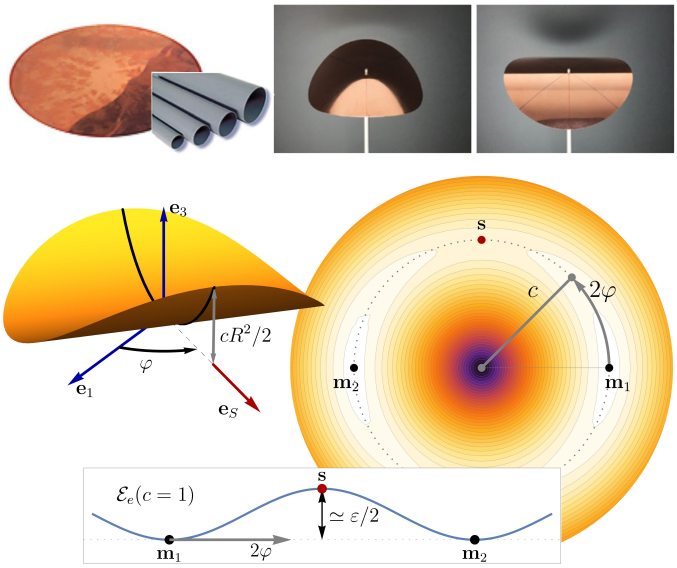

FIG. 1. Top: the initially flat copper disk and the two stable equilibrium shapes after the plastic deformations. Center: the current cylindrical shape is described by the curvature amplitude c and direction φ; the plot shows the elastic energy landscape in polar coordinates c and 2φ, with the two energy minima $\mathbf{m}_{1,2}$ ($c = 1$, $\varphi = 0, \pi/2$) and the two saddle points $\mathbf{s}_{1,2}$ ($c = (1+\varepsilon)^{-1}$, $\varphi = \pm\pi/4$). Bottom: the energy barrier between the two minima along the circle $c \simeq 1$, proportional to ε, a small dimensionless parameter related to material and geometrical imperfections.

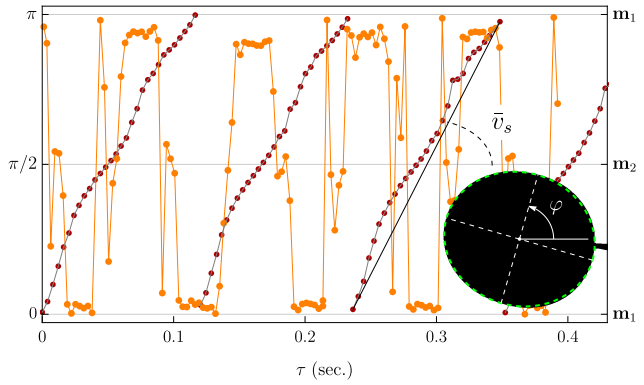

FIG. 2. Two recorded histories in the forced response in terms of curvature direction $\varphi(\tau)$ obtained with amplitude $W = 2.3$ mm but different forcing frequencies f. The orange curve displays an irregular pattern with quasi-periodic jumps for $f \simeq 0.86 f_0$. The dark red curve indicates a regular periodic motion with almost constant precession speed for $f \simeq 0.92 f_0$. The inset displays a shell image as recorded by the high-frequency camera lying on the vertical of the shaker: in every frame the shell boundary is fitted to an ellipse (green) to estimate the current values of c and φ. Videos are available in [2].

small stiffness to the material anisotropy. The nontrivial dynamics results from the nonlinear inertial coupling between the transverse oscillations and the soft bistable mode associated to the precessions of the curvature axis. That may open up the way to new applications of morphing structures in dynamics, as for the design of energy harvesting devices [4, 12].

EXPERIMENTAL PROTOTYPE

The experimental prototype of vanishing-stiffness shell is fabricated by winding an initially flat disk of radius $R = 122.5\,\text{mm}$ and thickness $h = 0.3\,\text{mm}$ over PVC cylinders of progressively smaller diameters, up to a minimal radius of curvature 110 mm. This process induces an isotropic plastic curvature [18]. The disk is made of nominally isotropic copper (Cua1H14) with Young modulus $Y = 124\text{GPa}$, Poisson ratio $\nu = 0.33$, mass density $\rho = 9690\text{Kg}\,\text{m}^{-3}$. After several winding cycles along many radial directions, the shell presents two stable cylindrical configurations of almost uniform curvature, marked by the points $\mathbf{m}_1$ and $\mathbf{m}_2$ in Fig. 1. The orientations of their curvature axes are mutually orthogonal, whilst their radii of curvature are approximately equal to $R_0 = 178 \pm 2\text{mm}$. The direct manipulation of the shell reveals a stiff bending mode and a soft deformation mode associated with the rotation of the curvature axis. In the following, we will refer to the soft mode as *zero-stiffness* or *neutrally stable* modes, see also [11, 17, 18, 26**?** **?**]

To study the system dynamics, we have clamped the center of the shell on a shaker (Bruel&Kjaer 4809) and imposed an harmonic seismic oscillation of the mounting point in the form $\bar{w}(\tau) = W \sin 2\pi f \tau$. To measure the time-histories of curvature amplitude $c(\tau)$ and direction $\varphi(\tau)$, we have recorded the shell motion with a camera giving a top view of the shell. For every frame, we used an image recognition tool to fit the shell boundary to an ellipse (dashed green in the inset of Fig. 2). The direction of the minor axis of the fitted ellipse gives the value of φ at that instant. The curvature is inferred from the ratio of the axis lengths. For small values of the amplitude W, the shell experienced small oscillations near the stable equilibria. For both $\mathbf{m}_1$ or $\mathbf{m}_2$ we have measured a natural frequency $f_0 = 18 \pm 0.3\text{Hz}$ and a damping factor $\zeta \simeq 0.03$. When increasing the forcing amplitude W the rotation of the curvature axis starts to be visible. One progressively observes transitions between the two stable equilibria, eventually associated with the continuous precession of the curvature direction φ or with an intermittent dynamics, see the experimental videos in [2]. The diagrams in Fig. 2 show two typical time-histories for the curvature direction φ. In the orange curve ($f = 15.5$ Hz) the transition between the stable equilibria $\mathbf{m}_1$ ($\varphi = 0 \equiv \pi$) and $\mathbf{m}_2$ ($\varphi = \pi/2$) is chaotic. The dark red curve ($f = 16.35$ Hz) corresponds to a regular precession of the curvature direction with at an almost constant speed $d\varphi(\tau)/d\tau$ of about $\pi/(0.122\,\text{s}) \simeq 25.7\,\text{rad/s}$.

UNIFORM CURVATURE SHELL MODEL

To develop an analytical model, we consider the object as an inextensible Koiter shell with curvature uniform in space [10]. Let $(O, \mathbf{e}_1, \mathbf{e}_2, \mathbf{e}_3)$ be an orthonormal fixed reference frame (see Figure 1). Hence, the curvature is described by a rank-one 2×2 symmetric tensor $\mathbf{k}(c,\varphi) = (c/R_0)\ \mathbf{e}_S(\varphi) \otimes \mathbf{e}_S(\varphi)$ with $\mathbf{e}_S(\varphi) = \cos\varphi\,\mathbf{e}_1 + \sin\varphi\,\mathbf{e}_2$, where c is the dimensionless curvature amplitude, φ the orientation of the curvature axis, and $\otimes$ denotes the usual tensor product. After the initial plastic forming process, the material behavior is linearly elastic, but slightly anisotropic. Denoting by $\mathbf{1}$ the identity tensor, the target plastic curvature is $\mathbf{k}_p = \mathbf{1}/R_p$. The elastic misfit is $\mathbf{k}_{\text{el}} = \mathbf{k} - \mathbf{k}_p$ and the elastic energy density per unit of surface is

$$\frac{D}{2}\left((1-\nu)\,\|\mathbf{k}_{\text{el}}\|^2 + \nu\,\text{Tr}(\mathbf{k}_{\text{el}})^2 + \varepsilon\,(\mathbf{k}_{\text{el}}\,\mathbf{e}_1\cdot\mathbf{e}_2)^2\right)$$

where $\|\mathbf{k}\|^2 = k_{ij}k_{ji}$ and $D := Yh^3/(12(1-\nu^2))$ is the bending modulus and ε introduces the effect of a small material anisotropy, that we attribute to the anisotropic plastic hardening. Integrating over the shell surface, the elastic potential energy reads

$$\mathcal{V}(c,\varphi) = V_0\left(\frac{c^2}{2}\left[1+\frac{\varepsilon}{2}(1-\cos 4\varphi)\right] - c\right) + const, \quad (1)$$

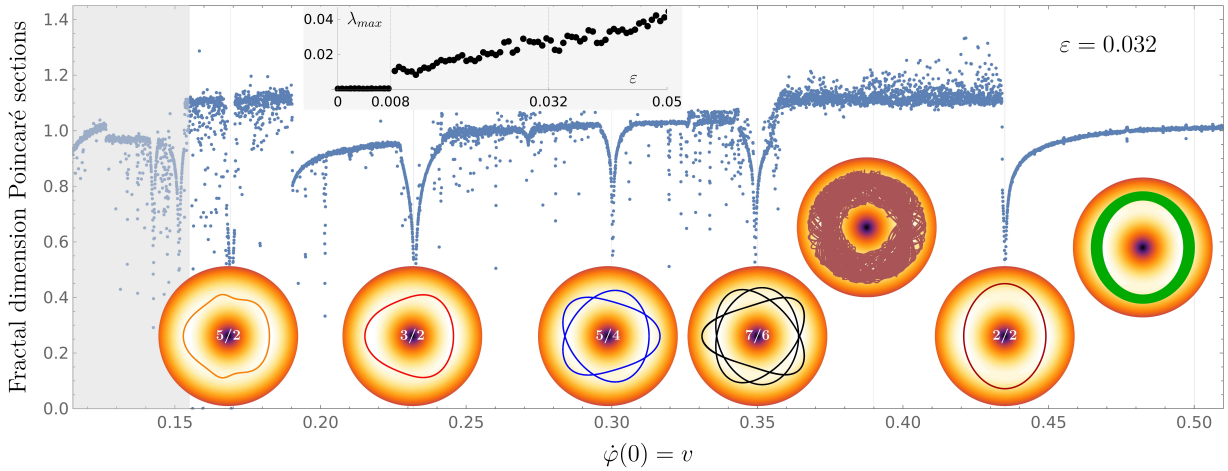

FIG. 3. Free undamped response of Eq.(4) with $\varepsilon = 0.032$: fractal dimension of the Poincaré sections as function of the initial precession speed (blue points), for initial conditions $\varphi(0) = \dot c(0) = 0$, $c(0) = 1$, $\dot\varphi(0) = v$. For the seven representative values of v (thin vertical lines), the insets display the trajectories in polar coordinates $(c, 2\varphi)$. Periodic motions are marked with their ratio n/k denoting the number n of oscillations in c for passing from $\varphi = 0$ to $\varphi = k\pi/2$. The gray region on the left distinguishes the minimal initial speed $v^* \simeq \sqrt{3\varepsilon}/2 \simeq 0.15$ to reach the saddle point **s** and to escape from the initial energy well. The Lyapunov exponent in the top inset indicates a chaotic behavior for $\varepsilon > 0.008$.

where $V_0 = \frac{\pi h^3 Y R^2}{12 R_0^2}$. In Fig. 1 the shell elastic energy is plotted in the plane where c is the radial coordinate and 2φ the angular coordinate. The energy barrier between the saddle points and the minima is

$$\mathcal{V}\left(\frac{1}{1+\varepsilon}, \frac{\pi}{4}\right) - \mathcal{V}(1,0) = \frac{\varepsilon}{2(1+\varepsilon)} V_0. \qquad (2)$$

In the ideal case of a perfectly isotropic shell ($\varepsilon = 0$), the elastic energy is independent of the orientation φ of the axis of curvature, see the inset in Fig. 1. This justifies the appellation "zero-stiffness" given in [17] as the shell equilibrium is indifferent to variations of φ. In the physical object, the imperfections lead to positive values of the parameter ε and to a bistable behavior. Relating the value of the imperfection to the margin of stability of the two stable equilibria we have measured $\varepsilon \simeq 0.032 \pm 0.005$ [18]. Under the same assumptions used to derive the elastic energy, the leading term of the kinetic energy of the shell is found to be $\mathcal{T}(c, \dot c, \dot\varphi) = (\frac{\dot c^2}{2} + \frac{2}{3} c^2 \dot\varphi^2) V_0$ where the superimposed dot denotes the derivative with respect to a dimensionless time $t := \Omega_0 \tau$, with $\Omega_0 = h\sqrt{20Y/\rho}/(3R^2)$. The dimensionless Lagrangian of our two degree-of-freedom model reads as

$$\mathcal{L} = \frac{\dot c^2}{2} + \frac{2c^2\dot\varphi^2}{3} - \frac{c^2}{2}\left[1 + \frac{\varepsilon(1-\cos 4\varphi)}{2}\right] + c. \qquad (3)$$

The structural and acoustic damping is modeled by a Rayleigh dissipation function $\mathcal{R} = \delta(\dot c^2/2 + 2c^2\dot\varphi^2/3)$, where δ is a dimensionless damping coefficient. Hence, modeling the effect of the shaker as an harmonic seismic forcing of dimensionless amplitude $A = \frac{40 R_0 W}{9R^2}$ and frequency $\omega = \Omega/\Omega_0$, the equations of motions read as:

$$\begin{aligned} &\ddot c + \delta\dot c + c\left(1 - \frac{\varepsilon(1-\cos 4\varphi)}{2}\right) - \frac{4c\dot\varphi^2}{3} = 1 + A\omega^2 \sin\omega t, \\ &\frac{d}{dt}\left(\frac{4c^2\dot\varphi}{3}\right) + \delta\,\frac{4c^2\dot\varphi}{3} + \varepsilon\, c^2 \sin 4\varphi = 0. \end{aligned} \qquad (4)$$

We refer the reader to the Supplemental Material, section I, for a detailed derivation of the model equations.

FREE UNDAMPED DYNAMICS

We start looking at the undamped free response ($\delta = 0$, $A = 0$) of the associated Hamiltonian system, for which the total energy $\mathcal{H} = \mathcal{T} + \mathcal{V}$ is conserved and constitutes a first integral. In the perfect case ($\varepsilon = 0$), the angular momentum $p_\varphi = 4c^2\dot\varphi/3$ is also conserved, and the system reduces to a one-dimensional oscillator in the c variable under the action of the effective potential $\mathcal{V}_{\rm eff}(c) = c^2/2 - c + 3p_\varphi^2/8c^2$. The system is integrable, its dynamics is diffeomorphic to a 2-dimensional torus and chaos is not possible [3, 7]. Motions with precession of the curvature axis at constant speed v and curvature amplitude c_v are possible for initial conditions $\dot\varphi(0) = v$, $\dot c(0) = 0$, $c(0) = c_v = \frac{1}{1-4v^2/3}$, where c_v is the minimum of the effective potential $\mathcal{V}_{\rm eff}$. Small oscillations around this equilibrium are in the form

$$c(t) = c_v + a\sin\omega_v t, \;\; \varphi(t) = vt + \frac{2av}{\omega_v c_v}(1 - \cos\omega_v t) \qquad (5)$$

with $a \ll 1$ and $\omega_v = \sqrt{\mathcal{V}''_{\rm eff}(c_v)} = \sqrt{1+4v^2}$. Since φ is a $\frac{\pi}{2}$-periodic angular variable, see (3), a countable

family of periodic solutions $(c,\varphi)_{n/k}$, with integer n and k, are possible for precession speeds $v_{n/k} = \frac{k}{4n}\omega_v = \pm 1/(2\sqrt{4n^2/k^2-1})$, see the Suppemental Material [2], Section 2. This kind of periodic solutions are key to understand the free and forced response of the imperfect system.

To investigate the imperfect system, we numerically integrate the governing equations (4) with $\varepsilon = 0.032$, varying the initial condition $\dot{\varphi}(0) = v$. For each v, we calculate the fractal dimension [7] of the Poincaré sections in the hyperplane $\varphi = \pi/2$, see Fig. 3. The details on the numerical methods used are reported in the supplemental material [2]. The dimension of the attractor tells that a chaotic dynamics is possible. The onset of global chaos is analyzed through the maximal Lyapunov exponent, $\lambda_{\max}$, which proves a possible chaotic behavior for sufficiently large imperfections ($\varepsilon \gtrsim 0.01$), and notably for the experimental value used. Yet, some stable quasi periodic motions are experienced, as shown by the points with vanishing fractal dimension. As shown in the insets in Fig. 3, consistently with the KAM theory [3], the lowest-order periodic orbits, $(c,\varphi)_{n/k}$ in (5) obtained for $\varepsilon = 0$, persist almost unchanged in the imperfect system [2, Fig. 4].

FORCED DYNAMICS

The free undamped response shows that the almost zero-stiffness deformation mode implies the presence of periodic solutions with continuous precessions of the curvature axis. In the damped physical system, the dissipation is not negligible and an external excitation $A > 0$ is necessary to observe them experimentally. Figure 4 reports the numerical results for the forced damped evolution, using the experimentally identified value of the damping factor $\delta \simeq 3\%$. For each value of the forcing amplitude A and frequency ω, we integrate numerically (4) for a sufficiently long time interval $t_{max} \sim 10^3$ and plot the ratio between the average precession speed $\bar{\dot{\varphi}}$ and the forcing frequency ω, neglecting the initial transient response [2]. Around the basic bending frequency $f_0 = \sqrt{5}h/(3\pi R^2)\sqrt{Y/\rho}$, the contour plot shows the existence of a large yellow region, where $\bar{\dot{\varphi}} = \omega/4$. This regime corresponds to the periodic motions with a regular precession of the curvature axis. The numerical results are consistent with the experimental points E_{1-6} in the plane (ω,A) for which such continuous precession regimes were observed. These periodic solutions are as the free periodic motion (5), but with the oscillating frequency ω_v replaced by the forcing frequency ω. They have a well-defined precession speed $v_{2/2} = \omega/4$, corresponding to a locking condition with $n = 2$ c-oscillations for a full precession of the curvature axis, $k = 2$. Higher harmonics are in principle possible but not visible experimentally. The central region with the regular precession regime is surrounded by chaotic dynamics where the curvature axis intermittently oscillates between the two energy wells as displayed by numerical and experimental trajectories, which are in a reasonable agreement in all cases. For small forcing amplitudes (case N_1), the result of the forced motion are small oscillations in c without rotation of the curvature axis ($\varphi \simeq 0$). The cubic nonlinearity renders these solutions unstable for sufficiently large amplitudes. We have performed the stability analysis of the periodic solution with $\varphi = 0$, which provides the marginal curve $A_s(\omega)$ in the contour plot of Fig. 4 [see 2]. For $A > A_s(\omega)$, finite amplitude oscillations in φ are found. Depending on the available energy, they can trigger a transition from intra-well oscillations around

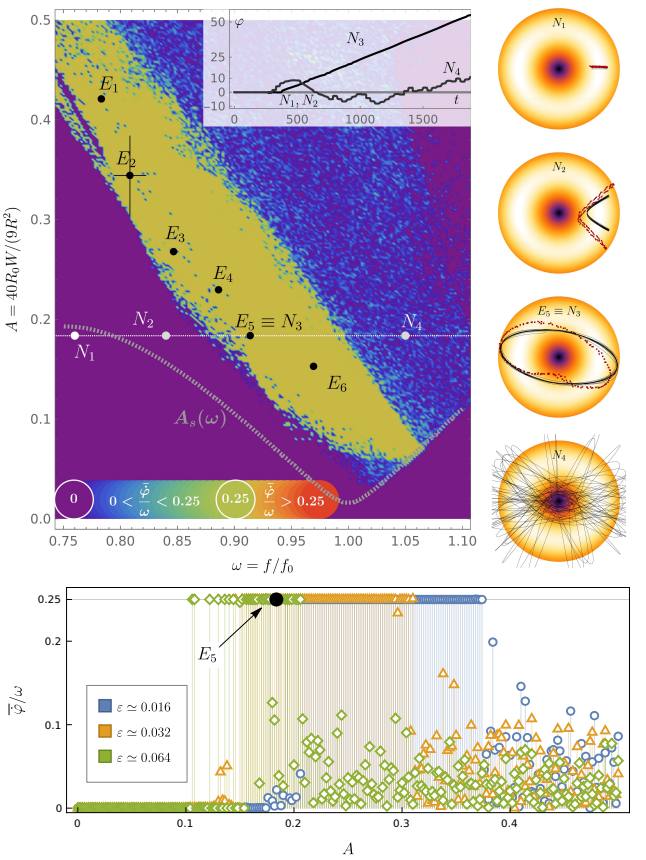

FIG. 4. Top-left: Contour plot for the ratio between the asymptotic precession speed $\bar{\dot{\varphi}}$ and ω as a function of the forcing amplitude A and frequency ω found with direct integration of Eqns. (4) for $\varepsilon = 0.032$ and $\delta = 3\%$. The yellow region with $\bar{\dot{\varphi}} = \omega/4$ corresponds to the regular precession of the curvature axis and is consistent with the experimental observation of regular motions (points E_{1-6}). Top-right: Trajectories in the polar coordinates $(c, 2\varphi)$ at different frequencies, corresponding to the points N_{1-4}: numerical (black) and experimental (dark-red); the corresponding time histories are reported in the top inset. Bottom: Cross section of the contour-plot above for $\omega = 0.92$ and for three different imperfection values.

$\varphi = 0$, as shown by the trajectories N_2, to cross-well motions, including the solutions with continuous precession of the curvature axis, as $E_5 \equiv N_5$ and intermittent chaotic oscillations, as N_4. A particularly intriguing feature of the nonlinear dynamics is that the transversal seismic forcing in the c variable results in regular precessions of the angular variable φ. The bottom of Fig. 4 shows that the precession speed, in the yellow region, is locked to the value $\omega/4$ independent of the forcing amplitude, the imperfection value and the damping factor [2, Fig. 6]. The insets of Figure 4 shows that the experimental trajectories in red are asymetric, because of the imperfections present in the tested shell. This symmetry breaking determines the direction of the precession in the experiments [see the video in 2].

CONCLUSIONS

We have shown that prestressed cylindrical shells with floppy deformation modes exhibit an intriguing dynamics including regular the precession or the intermittent oscillations of their curvature axis. Our minimal two degrees-of-freedom model traces back the observed behavior to the nonlinear inertial coupling between the soft bistable mode associated to the rotation of the curvature axis and the stiff mode associated to the variations of the curvature amplitude. The presence of the soft mode is due to the competition between the prestress, that promotes a spherical curvature, and the geometrical nonlinear effects, that constrains the thin elastic shell to remain almost cylindrical, without assigning any preferential orientation of the curvature axis. The non-vanishing stiffness of the soft mode is related to a small material anisotropy. Breaking the rotational symmetry, this non-vanishing stiffness produces the bistable behavior and it is essential to explain the chaotic dynamics. We have characterized the regular regimes as persistent periodic solutions of the perfect system, showing that their average precession speed is precisely determined by a locking condition with the transverse oscillation forcing frequency f, being constant for a large span of amplitudes:

$$\overline{\frac{d\varphi}{d\tau}} = \frac{2\pi f}{4} = \frac{\pi}{2}\, f. \tag{6}$$

The reported behavior is independent of the length-scale and can easily be replicated. That opens up the way to the design of energy harvesting devices at microscopic and macroscopic scales exploiting almost neutrally stable manifolds. The presence of floppy modes that allows for controllable shape-change is the characteristic feature of morphing structures, as pre-stressed annular rings [21, 25] or degenerate meta-materials [9, 23]. This gives them specific properties, as the ability to support low-energy fractional excitations [30]. Our results constitute a first step in unveiling the influence of soft modes in the structural dynamics. Our minimal model can constitute also a novel case-study for the illustration of surprising nonlinear effects in Hamiltonian mechanics.

[1] *Rolatube Technology Ltd, see rolatube.com.*

[2] See Supplemental Material at [url will be inserted by publisher].

[3] V.I. Arnold. *Mathematical methods of classical mechanics*. Springer, 2013.

[4] A. F. Arrieta, P. Hagedorn, A. Erturk, and D. J. Inman. A piezoelectric bistable plate for nonlinear broadband energy harvesting. *Applied Physics Letters*, 97(10):104102, 2010.

[5] M. Brunetti, S. Vidoli, and A. Vincenti. A class of morphing shell structures satisfying clamped boundary conditions. *International Journal of Solids and Structures*, 82:47 – 55, 2016.

[6] Y. Cao, M. Derakhshani, Y. Fang, G. Huang, and C. Cao. Bistable structures for advanced functional systems. 31(45):2106231, aug 2021.

[7] M. Cencini, F. Cecconi, and A. Vulpiani. *Chaos: from simple models to complex systems*. World Scientific, 2010.

[8] Z. Chen, Q. Guo, C. Majidi, W. Chen, D.J. Srolovitz, and M.P. Haataja. Nonlinear geometric effects in mechanical bistable morphing structures. *Phys. Rev. Lett.*, 109:114302, 2012.

[9] Gary P. T. Choi, Levi H. Dudte, and L. Mahadevan. Programming shape using kirigami tessellations. 18(9):999–1004, aug 2019.

[10] Philippe G Ciarlet. An introduction to differential geometry with applications to elasticity. *Journal of Elasticity*, 78(1):1–215, 2005.

[11] G. Corsi, A. De Simone, C. Maurini, and S. Vidoli. A neutrally stable shell in a stokes flow: a rotational taylor's sheet. *Proceedings of the Royal Society A: Mathematical, Physical and Engineering Sciences*, 475(2227):20190178, 2019.

[12] F. Cottone, H. Vocca, and L. Gammaitoni. Nonlinear energy harvesting. *Physical Review Letters*, 102(8):080601, 2009.

[13] J. Dervaux and M. Ben Amar. Morphogenesis of growing soft tissues. *Phys. Rev. Lett.*, 101:068101, 2008.

[14] Y Forterre, J M Skotheim, J Dumai, and L Mahadevan. How the venus flytrap snaps. *Nature*, 433:421–425, 2005.

[15] M. Gomez, D.E. Moulton, and D. Vella. Critical slowing down in purely elastic 'snap-through' instabilities. *Nature Physics*, 13(2):142–145, 2017.

[16] A. Goriely and M. Ben-Amar. Differential growth and instability in elastic shells. *Physical Review Letters*, pages 198103,1–4, 2005.

[17] S.D. Guest, E. Kebadze, and S. Pellegrino. A zero-stiffness elastic shell structure. *Journal of Mechanics of Materials and Structures*, 6(1-4):203–212, 2011.

[18] W. Hamouche, C. Maurini, S. Vidoli, and A. Vincenti. Multi-parameter actuation of a neutrally stable shell: a flexible gear-less motor. *Proceedings of the Royal Society A*, 473(2204):20170364, 2017.

[19] R.L. Harne and K.W. Wang. A review of the recent research on vibration energy harvesting via bistable systems. *Smart Materials & Structures*, 22(2):023001, 2013.

[20] E. Kebadze, S.D. Guest, and S. Pellegrino. Bistable prestressed shell structures. *International Journal of Solids and Structures*, 41(11-12):2801–2820, 2004.

[21] D.E. Moulton, T. Lessinnes, and A. Goriely. Morphoelastic rods. part i: A single growing elastic rod. 61(2):398–427, feb 2013.

[22] J.-H. Na, N.P. Bende, J. Bae, C.D. Santangelo, and R.C. Hayward. Grayscale gel lithography for programmed buckling of non-euclidean hydrogel plates. *Soft Matter*, 12:4985–4990, 2016.

[23] G. Noselli, M. Arroyo, and A. DeSimone. Smart helical structures inspired by the pellicle of euglenids. 123:234–246, feb 2019.

[24] M. Pezzulla, G.P. Smith, P. Nardinocchi, and D.P. Holmes. Geometry and mechanics of thin growing bilayers. *Soft Matter*, 12:4435–4442, 2016.

[25] M. Schenk and S. D Guest. On zero stiffness. 228(10):1701–1714, nov 2013.

[26] K.A. Seffen and S.D. Guest. Prestressed Morphing Bistable and Neutrally Stable Shells. *Journal of Applied Mechanics*, 78(1), 10 2010.

[27] Keith A. Seffen and Corrado Maurini. Growth and shape control of disks by bending and extension. *Journal of the Mechanics and Physics of Solids*, 61(1):190–204, 2013.

[28] E. Sharon and E. Efrati. The mechanics of non-euclidean plates. *Soft Matter*, 6:5693–5704, 2010.

[29] S.C. Stanton, C.C. McGehee, and B.P. Mann. Nonlinear dynamics for broadband energy harvesting: Investigation of a bistable piezoelectric inertial generator. *Physica D: Nonlinear Phenomena*, 239(10):640 – 653, 2010.

[30] K. Sun and X. Mao. Fractional excitations in non-euclidean elastic plates. *Phys. Rev. Lett.*, 127:098001, Aug 2021.

[31] S. Waitukaitis, R. Menaut, B.G. Chen, and M. van Hecke. Origami multistability: From single vertices to metasheets. *Phys. Rev. Lett.*, 114:055503, 2015.

Dynamics of a shapeable object with a vanishing-stiffness mode: supplemental material

Sergio Chibbaro

Sorbonne Université, CNRS, UMR 7190,

Institut Jean Le Rond d'Alembert, F-75005 Paris, France

Corrado Maurini

Sorbonne Université, CNRS, UMR 7190,

Institut Jean Le Rond d'Alembert, F-75005 Paris, France

Stefano Vidoli

Dipartimento di Ingegneria Strutturale e Geotecnica,

Sapienza Università di Roma, Italy

Angela Vincenti

Sorbonne Université, CNRS, UMR 7190,

*Institut Jean Le Rond d'Alembert, F-75005 Paris, France**

* Your e-mail address; Your web page

I. DERIVATION OF THE MODEL

To the derive the shell elastic energy we consider the shell as *inextensible*. For sufficiently thin shells this hypothesis is well justified, see [**?**]. Starting from a flat natural configuration and recalling classical results in the theory of shells, see *e.g.* [**?**], the inextensibility hypothesis implies that the Gaussian curvature is everywhere constant and vanishing. Hence the curvature field $\mathbf{k}$ is a field of rank-one 2×2 symmetric matrices, namely $\mathbf{k} = \mathbf{k}(\tilde{c}, \varphi) = \tilde{c}\ \mathbf{e_S}(\varphi) \otimes \mathbf{e_S}(\varphi)$ for some real $\tilde{c}$ and some angle φ. Here $\mathbf{e_S} = (\cos\varphi, \sin\varphi)$ means the curvature direction, see Fig. **??**. Justified by the experimental evidence, we further assume that the curvature $\tilde{c}$ and the curvature direction φ do depend on time but are spatially uniform; thus, at every instant τ, the shell configuration is cylindrical and described by the two Lagrangian parameters $\tilde{c}(\tau) \in [0, \infty)$ and $\varphi(\tau) \in [0, 2\pi)$. The shell being inextensible, the elastic energy V is reduced to the bending contribution only; assuming the shell as linearly elastic we have

$$V = \frac{1}{2} \int_\Omega \mathbb{D}(\mathbf{k} - \bar{\mathbf{k}}) \cdot (\mathbf{k} - \bar{\mathbf{k}})\, d\Omega, \qquad \Omega := \{r(\cos\theta, \sin\theta), 0 \le r \le R, \theta \in [0, 2\pi)\} \tag{1}$$

with $\bar{\mathbf{k}} = \bar{k}_p \mathbf{1}$ the isotropic plastic deformation imposed by the winding process and $\mathbb{D}$ is the bending stiffness tensor

$$\mathbb{D}\mathbf{k} = D\left((1-\nu)\,\mathbf{k} + \nu(\mathrm{Tr}\mathbf{k})\,\mathbf{1} + \varepsilon\,(\mathbf{k}\mathbf{e}_1 \cdot \mathbf{e}_2)\,\frac{\mathbf{e}_1 \otimes \mathbf{e}_2 + \mathbf{e}_2 \otimes \mathbf{e}_1}{2}\right). \tag{2}$$

Here $D := Yh^3/(12(1-\nu^2))$ is the bending stiffness, Y the Young modulus, h the shell thickness, $\mathbf{1}$ the 2×2 identity tensor and Tr the trace operator. Due to ε parameter, the material is orthotropic with Poisson ratio ν: indeed, the material shear stiffness is $D((1-\nu)/2 + \varepsilon)$, $D(1-\nu)/2$ being the usual isotropic value. From (1) one gets

$$V = \frac{\pi R^2 h^3 R_0^2 Y}{12}\left(\frac{c^2}{2}\left[1 + \frac{\varepsilon}{2}(1 - \cos 4\varphi)\right] + (1-c)\,(1+\nu)\right) \tag{3}$$

where we have introduced the dimensionless curvature $c := \tilde{c}/R_0$. Once dropped the constant term and rescaled, (3) reads to $V(c, \varphi) = c^2/2(1 + \varepsilon(1 - \cos 4\varphi)/2) - c\,(1+\nu)$, see Sect. **??** in the paper. The elastic energy V has two wells

$$\mathbf{m}_1 : (\varphi = 0, c = 1+\nu), \quad \mathbf{m}_2 : (\varphi = \pi/2, c = 1+\nu), \tag{4}$$

and two saddle points $\mathbf{s} : (\varphi = \pm\pi/4, c = (1+\nu)/(1+\varepsilon)$. The energy gap between the saddle points and the minima

$$V(\mathbf{s}) - V(\mathbf{m}_1) = \frac{\varepsilon(1+\nu)^2}{2(1+\varepsilon)}, \tag{5}$$

vanishes for vanishing imperfections. In the ideal case $\varepsilon = 0$ of a perfectly isotropic shell, the elastic energy is flat along the circle $c = 1 + \nu$. This justifies the appellation "zero-stiffness" given in [**?**] as the shell equilibrium is indifferent to variations of φ. In reality imperfections, in the material or in the imposed plastic deformations, leads to positive values of the parameter ε: in our shells we have measured $\varepsilon \simeq 0.03 \pm 0.005$. Despite the fact that, when $\varepsilon > 0$, the curvature in the saddle is slightly different from the curvature in the minima, one can easily check that the maximal energy gap along the circle $c = 1 + \nu$ still scales as $O(\varepsilon)$. Hence, in any configuration the stiffness to variations of the curvature direction is $\partial_{\varphi\varphi} V = O(\varepsilon)$, but the stiffness to variation of the curvature is $\partial_{cc} V = O(1)$; the actual shell is bistable with the energy barriers $O(\varepsilon)$ or $O(1)$ depending on the path connecting the wells.

The kinetic energy is computed once known the velocity field in terms of Lagrangian parameters. Let $\mathbf{x} = x_1\mathbf{e}_1 + x_2\mathbf{e}_2$ the generic position in the shell reference domain Ω and let $s(\tau) := \mathbf{x}/R_0 \cdot \mathbf{e}_\mathbf{S}(\varphi(\tau))$ a dimensionless abscissa in the curvature direction at time τ. Referring to Fig. **??**, it easily seen that the transverse w and inplane $\mathbf{v}$ displacement fields respectively are

$$w = h_p^{-1}(1 - \cos(cs))/c, \qquad \mathbf{v} = v\,\mathbf{e}_\mathbf{S}(\varphi), \quad v = h_p^{-1}(\sin(cs)/c - s). \tag{6}$$

We derive these expressions recalling that c but also s by means of φ are function of time, to get velocity fields $\dot{w}$ and $\dot{\mathbf{v}}$. Hence we compute the shell kinetic energy by

$$T = \frac{1}{\tau_c^2} \int_\Omega \rho\, h\, (\dot{w}^2 + \dot{\mathbf{v}} \cdot \dot{\mathbf{v}})\, d\Omega \tag{7}$$

where ρ is the density per unit volume and the dots indicate derivatives with respect to the dimensionless time scale $t = \tau/\tau_c$. To obtain a closed form result we use power series of (6) in term of c to get:

$$T = \frac{3\pi\, R^6 h\, \rho}{80\tau_c^2 R_0^2} \left(\left(1 + \frac{50R^2}{189R_0^2} c^2 + O(c^3) \right) \frac{\dot{c}^2}{2} + \left(1 + \frac{5R^2}{36R_0^2} c^2 + O(c^3) \right) \frac{2}{3} c^2 \dot{\varphi}^2 \right). \tag{8}$$

Since for our shell $R \simeq 0.1225\,\mathrm{m}$ and $R_0 \simeq 0.175\,\mathrm{m}$, we note that the two dimensionless terms of order c^2 are both small with respect to 1 even if $c = O(1)$. Therefore, we neglect the higher order terms in c (this assumption corresponding to the adoption of a shallow-shell kinematics) and suitably rescale the kinetic energy to obtain the expression used in the paper $T(c; \dot{c}, \dot{\varphi}) = \dot{c}^2/2 + (2/3)\, c^2 \dot{\varphi}^2$. When the shell is forced by the shaker the kinetic

energy is computed similarly by adding the shaker imposed motion, $w_M(\tau) = W\,\sin(2\pi f\tau)$, to the transverse displacement $(6)_1$. The elastic and kinetic energy can be rescaled by the same term choosing a suitable time scale, namely $\tau_c = 3R^2/h\sqrt{\rho/(20Y)}$. With the Young modulus and density of copper and a thickness of about $h \simeq 0.3\,\mathrm{mm}$ we have $\tau_c \simeq 0.01\,\mathrm{s}$.

The Lagrangian in dimensionless form is therefore:

$$L(c,\varphi;\dot{c},\dot{\varphi}) = T - V = \frac{\dot{c}^2}{2} + \frac{2}{3}\,c^2\dot{\varphi}^2 - \frac{c^2}{2}\left(1 + \varepsilon\,\frac{1-\cos 4\varphi}{2}\right) + c\,(1+\nu) + A\,\alpha\cos(\alpha t)\dot{c}. \quad (9)$$

where $A := \frac{40WR_0}{9\tau_c^2R^2}$ is the dimensionless amplitude and $\alpha := 2\pi f\tau_c$ the dimensionless frequency. The equations of motion are easily computed to get

$$\ddot{c} + c\left(1 - \frac{\varepsilon}{2} + \frac{\varepsilon}{2}\cos(4\varphi)\right) - 1 - \nu - \frac{4c\dot{\varphi}^2}{3} = A\alpha^2\sin(\alpha t),\ \frac{d}{dt}\left(\frac{4c^2\dot{\varphi}}{3}\right) = -\varepsilon c^2\sin(4\varphi). \quad (10)$$

Using Hamilton formalism, we define the generalized coordinates $\mathbf{q} = \{c,\,\varphi\}$ and the conjugate momenta $\mathbf{p} = \{p_c,\,p_\varphi\} = \{\dot{c},\,4c^2\dot{\varphi}/3\}$. The free dynamics of our shell is governed by the Hamiltonian

$$H(c,\varphi;p_c,p_\varphi) = \frac{p_c^2}{2} + \frac{c^2}{2} - c\,(1+\nu) + \frac{3p_\varphi^2}{8c^2} + \varepsilon\frac{c^2}{4}(1-\cos 4\varphi), \quad (11)$$

or by the first-order ODEs

$$\dot{c} = p_c, \quad \dot{\varphi} = \frac{3p_\varphi}{4c^2}, \quad \dot{p}_c = 1 + \nu - c\left(1 - \frac{\varepsilon}{2} + \frac{\varepsilon}{2}\cos(4\varphi)\right) + \frac{3p_\varphi^2}{4c^3}, \quad \dot{p}_\varphi = -\varepsilon c^2\sin(4\varphi). \quad (12)$$

A. The integrable case

In absence of forcing $A = 0$ and for $\varepsilon = 0$, the shell has no preferred direction of curvature and the system is integrable by quadratures. Indeed, the Hamiltionan does not depend on φ and, therefore, the momentum $p_\varphi = 4c^2\dot{\varphi}/3$ is conserved. Moreover, the energy $E = \dot{c}^2/2 + c^2/2 - c\,(1+\nu) + 3p_\varphi^2/(8c^2)$ is conserved. We have two first integrals and, by the Arnold theorem [**?**], the motion is diffeomorphic to a 2-dimensional torus.

To solve the problem, we eliminate $\dot{\varphi} = 3p_\varphi/(4c^2)$ to obtain

$$\dot{c}^2 = 2(E - U(p_\varphi, c)), \quad \text{with} \quad U(p_\varphi, c) := \frac{3p_\varphi^2}{8c^2} + \frac{c^2}{2} - c\,(1+\nu). \quad (13)$$

or equivalently the following equation for the curvature:

$$\ddot{c}(t) + c(t) - (1+\nu) - \frac{3\,p_\varphi^2(t)}{4\,c(t)^3} = 0. \quad (14)$$

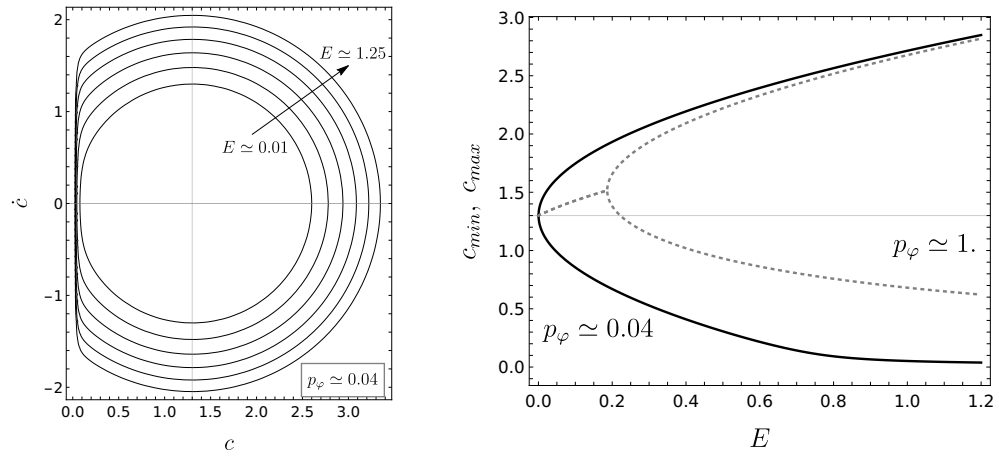

FIG. 1: The integrable case. Left) Eqn.(13) in the plane $(\dot{c}, c)$ for several values of the initial energy E and $F \simeq 0.05$. The vertical line labels the value $(1+\nu)$. Right) The maximal and minimal values of c as functions of the initial energy E. The bounds obtained for $p_\varphi \to 0$ remain valid when p_φ is increased.

Given the constant value of p_φ this is a nonlinear ODE in $c(t)$. It is interesting to remark that, if initially $\dot{c}(0) = 0$, one possible solution is a uniform precession at constant curvature, namely $c(t) = (1+\nu)/(1-4/3v_0^2)$ and $\varphi(t) = v_0\, t$. Here the effective potential well has been shifted from $c \simeq 1+\nu$ due to the angular momentum (a sort of centrifugal effect).

We also observe that, if $p_\varphi \neq 0$, then c must be strictly positive for the energy to be finite. The relation (13) between c and $\dot{c}$ is represented in Fig.1 on the left. It allows to compute the relation between t and c by a simple quadrature

$$t = \int_{c_0}^{c} \frac{1}{\sqrt{2(E - U(p_\varphi, x))}}\, dx, \tag{15}$$

The maximal and minimal values of c during these nonlinear oscillations can be computed solving for $\dot{c} = 0$ into (13). Figure 1 on the right displays such values. In particular the limit values of the curvature can be well approximated solving the problem with $p_\varphi = 0$ obtaining the bounds $0 \leq c \leq (1+\nu)\sqrt{2E + (\nu^2 - 1)}$, see Fig. 1 on the right.

II. NUMERICAL METHODS

For $\varepsilon > 0$, the shell is bistable with preferred direction of curvature at $\varphi = 0$ and $\varphi = \pi/2$; the system is no longer integrable and numerical experiments suggest an intricate dynamics between regular and irregular patterns. For $\varepsilon > 0$, the momentum p_φ is not conserved but,

as the system is autonomous, the total energy is still conserved, the perturbed system being quasi-integrable with two degrees of freedom, the KAM theorem assures the persistence of the integrable trajectories and, the KAM tori divides the space-phase, so that for a small enough perturbation the system should remain in a deformed integrable state.

Numerical evidence.

We have comprehensively analysed the system numerically solving the Hamilton equations corresponding to (11).

We have tested the free system response when the shell is initially placed at rest in the minimum $\mathbf{m}_1$ and is then perturbed by a precession velocity $\dot{\varphi}(0) = v_0$. In this case, the initial total energy is $E_0 = 2(1+\nu)^2 v_0^2/3$; equating this value to the elastic energy in the saddle we get $v_0^* = \sqrt{3\varepsilon}/2 + O(\varepsilon^{3/2})$ as the minimal initial precession speed for the system to explore the whole state space.

Starting from vanishing initial angular speed v_0, we numerically observe small oscillations around $\mathbf{m}_1$. These motions are superpositions of oscillations with dimensionless period $T = 2\pi$ in the c coordinate and oscillations with dimensionless period $\sqrt{3\,\varepsilon}\,T$ in the φ coordinate. The actual physical period for our shell is $\hat{T} = 2\pi/f_0 \simeq 0.35$ seconds, with $f_0 = 18$ Hertz the measured frequency of the small oscillations in c.

As the initial angular speed v_0 increases, these motions show an increasingly nonlinear character but the angular variable remains bounded $-\pi/2 < 2\varphi(t) < \pi/2$; refer to Fig. **??** to check that the other stable equilibrium position $\mathbf{m}_2$ is never reached. The minimal initial energy to break this bound is related to the elastic energy in the saddle, see Eq. (5), and, therefore scales as $O(\varepsilon)$.

Poincarè sections evidence

For every initial condition v_0, we have run a numerical simulation in the interval $t \in [0, 10^3\,T]$ recording the points $\mathcal{S}_{v_0} = \{(c(nT), p_c(nT), p_\varphi(nT)),\, n = 1, ...10^3\}$. As the phase space is four-dimensional and we have one conserved quantity, the set of points $\mathcal{S}_{v_0}$ in $\mathbb{R}^3$ represent the Poincarè section of our dynamical system associated to the initial pertubation v_0.

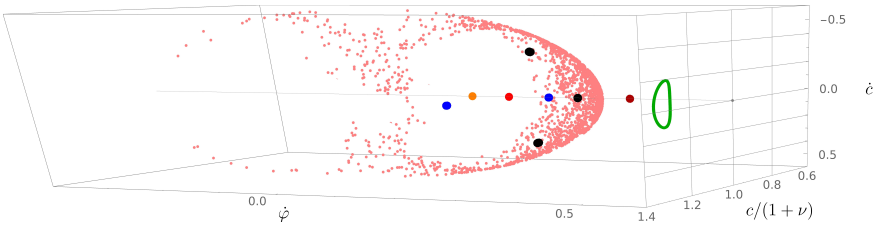

FIG. 2: Relevant Poincarè sections in the three-dimensional space (p_φ, c, p_c). These reduce to single points when $\dot{\varphi}(0) = 0.169, 0.232, 0.435$, respectively the orange, red and brown points. They reduce to two black (resp. three black) points when $\dot{\varphi}(0) = 0.3$ and $\dot{\varphi}(0) = 0.349$, to a cloud of green points $\dot{\varphi}(0) = 0.39$ and to the green curve when $\dot{\varphi}(0) = 0.5$.

Figure **??** plots, on a logarithmic axis, the volume of the smallest right parallelepiped containing $\mathcal{S}_{v_0}$. As Poincarè sections densely fill regions of the phase-space for chaotic motions and shrink to points when the motions are periodic, Fig. **??** allows for an overview of the system response for a wide range of initial precession speeds; therein v_0 ranges from 0.1 to 0.5 with steps of $2 * 10^{-5}$. The insets display the time-histories of $c(t)$ (radial coordinate) and $2\varphi(t)$ (angular coordinate) depicted as black curves over the elastic energy contours of Fig. **??**.

Already when the initial precession speed $v_0 \simeq 0.158$, slightly above the critival value $v_0^* \simeq 0.15$, we observe a region of chaotic motion followed by a small interval, around $v_0 \simeq 0.169$, where the motion is quasi-periodic. From $v_0 \sim 0.2$ to $v_0 \sim 0.35$ the character of the motions is also quasi-periodic. A large region of chaotic motion is observed from $v_0 \sim 0.35$ to $v_0 \sim 0.43$; then again at $v_0 \simeq 0.435$ the motion is almost periodic.

The three quasi-periodic motions, displayed in the insets of Fig. **??** at $v_0^{(1)} = 0.435$, $v_0^{(2)} = 0.232$, $v_0^{(3)} = 0.169$, corresponds to local minima of the Poincarè sections volume. These are characterized by precessions at almost constant speeds $\overline{\dot{\varphi}(t)} \sim \bar{v}^{(i)}$ and by functional relations, between curvature and curvature direction, in the form $c(\varphi) \simeq 1 + \nu - h^{(i)} \cos(2\, n^{(i)} \varphi)$ with $h^{(i)}$ three real values and $n^{(i)}$ three integers for $i = 1, 2, 3$.

For instance, when $v_0 = v_0^{(1)}$, the average precession speed is about $\bar{v}^{(1)} \simeq 0.326$ and $n^{(1)} = 2$ as the curvature is minimal twice (in $\mathbf{m}_1$ and $\mathbf{m}_2$) and maximal twice (in the saddles). Instead, at $v_0 = 0.232$ we have $\bar{v}^{(2)} \simeq 0.179$ and $n^{(2)} = 3$, whilst at $v_0 = 0.169$ one observes $\bar{v}^{(3)} \simeq 0.104$ and $n^{(3)} = 4$. It seems that the lower is the initial precession speed,

the more are the curvature oscillations in every complete precession of the curvature axis.

Remark also that in all the cases $\bar{v}^{(i)} < v_0^{(i)}$; this is to be expected because the system is conservative and the initial precession speed is the maximal possible, being applied in the system at rest in $\mathbf{m}_1$ where $\mathcal{E}_e$ is minimal.

Figure **??** displays a contourplot of the average precession speed $\bar{v} \equiv \overline{\dot{\varphi}}$ with respect to the initial precession speed v_0 and the imperfection parameter ε. When ε is vanishing, the system is regular and the dependence of the average velocity with respect to the initial one is smooth and monotonically increasing; the angle variable φ is always cyclic. However, for values of the perturbation parameter higher than $\varepsilon \sim 10^{-2}$, the average precession speed could suddenly drop; see, for instance, the region with almost triangular shape in the center of the plot. Therein the precession speed changes sign often during the observation period and this results in small overall value of its average. The dashed curves indicates the isolines where $\bar{v} = 0.16$, 0.24 and 0.43: at these speeds the motion seems to avoid chaos until very large imperfections values.

To corroborate quantitatively the onset of chaotic behavior at the critical value $\varepsilon \sim 10^{-2}$, we have computed the Lyapunov spectrum [**?** **?**]. Being the system autonomous and hamiltonian, only the largest Lyapunov exponent, say λ_{max}, is relevant. We start with the system at rest in the saddle, give random initial conditions and use the numerical algorithm [**?**], with $T_{max} = 2 \cdot 10^4$ and $dt = 0.05$, to numerically approximate λ_{max} as a function of ε. The result is displayed in the inset of Fig **??**: a neat transition to global chaos ($\lambda_{max} > 0$) is observed for $\varepsilon \gtrsim 0.008$, this picture being only marginally modified changing the initial energy over a large spectrum of values. For smaller values, it is found consistently that the system is not chaotic and the value of λ_{max} can be considered equal to zero, being of the same order of the numerical error.

III. DERIVATION OF THE MATHIEU EQUATION

a. Analytical estimates. The numerical evidence suggests a prominent role of the precessions within the zero-stiffness manifold. Particular values of the precession speed seem to be more stable and avoid chaotic behaviors, regardless of the value of the imperfection parameter. To understand the precise mechanism, we resort to a perturbative analysis and seek for solutions in the form $\varphi(t) = vt + o(\varepsilon)$. For such an ansatz the Lagrangian does not

depends on φ within an error $o(\varepsilon)$ and we are left with

$$\ddot{c}(t) + \left(1 + \frac{\varepsilon}{2} - \frac{4v^2}{3} - \frac{\varepsilon}{2}\cos(4tv)\right) c(t) = (1+\nu), \tag{16}$$

or, changing the time scale $t \to \tau/(4v)$, the Mathieu equation

$$c''(\tau) + \varpi^2 \left(1 - \eta\cos\tau\right) c(\tau) = \bar{c}, \tag{17}$$

where $\bar{c} := (1+\nu)/(16v^2)$, $\eta := 3\varepsilon/(3\varepsilon - 8v^2 + 6)$, $\varpi^2 := (3\varepsilon - 8v^2 + 6)/(96v^2)$ and a prime indicates differentation with respect to τ. The resonance condition of (17), namely $\varpi = k/2$ for $k = 1, 2, 3, ...$, leads to the resonant precession speeds

$$v^*_{k=1,2,3...} = \frac{\sqrt{6+3\varepsilon}}{2\sqrt{2}\sqrt{1+3k^2}} = \frac{\sqrt{3}}{2\sqrt{1+3k^2}} + O(\varepsilon). \tag{18}$$

Figure 3 displays the relation between the Mathieu pulsation ϖ and the precession speed v, comparing the critical values (18) with the numerical ones found in Fig. **??**.

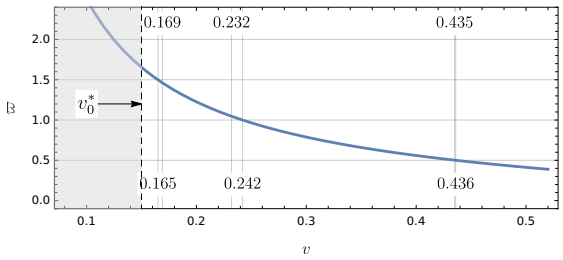

FIG. 3: The relation between the Mathieu pulsation ϖ and the precession speeds. For $\varpi = 0.5, 1, 1.5$ the corresponding values of critical speeds are $v = 0.165, 0.242, 0.436$. The higher resonances fall below the critical threshold v_0^*.

Hence, the three relevant

We have also performed a perturbative analysis where $\varphi = vt + O(\varepsilon)$; this simplified model is able to reproduce quite well all the regions except where chaos is present and the perturbation of the angle variable is of order one. Evidently, these regions increase in size with increasing the value of the anisotropy given by ε. The theoretical analysis confirms unambiguously that the dynamics is governed by parametric resonances, which stick the angle variable to remain periodic almost everywhere in the parameter space

To provide a stronger link with experiments and opening up the way to the precise control of the object, we have repeated the analysis introducing explicitly the forcing and a

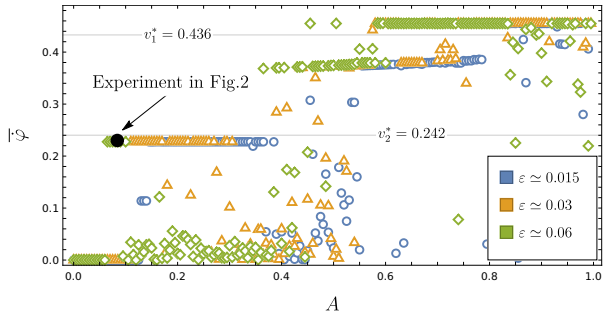

FIG. 4: Average precession speed in forced oscillationsas a function of the forcing amplitude A, for three different values of imperfections. The forcing frequency is fixed at $f = 0.91 f_0 = 16.4$ Hertz.

2% viscous dissipation. Results are displayed in Fig. 4: for small amplitudes, the system is trapped in a region around the inital position and cannot move freely. For an energy sufficient to overcome potential barrier, the resonance is activated and the average speed turns out to be around the Mathieu $k = 2$ resonance over a range of amplitudes. For large amplitudes, such that the energy landscape is basically irrelevant, the dynamics is found to be regular with average velocity given by Mathieu $k = 1$ resonance. Between the two resonances, there is a region of chaotic dynamics which depends on the imperfections. Remarkably, at experimental conditions it is found that the plate operate almost always with no-stifness dynamics.